doi:10.1038/nature14111

Segmented lateral dyke growth in a rifting event at Bárðarbunga volcanic system, Iceland

Freysteinn Sigmundsson[1], Andrew Hooper[2], Sigrún Hreinsdóttir[3], Kristín S. Vogfjörd[4], Benedikt G. Ófeigsson[4], Elías Rafn Heimisson[1], Stéphanie Dumont[1], Michelle Parks[1], Karsten Spaans[2], Gunnar B. Gudmundsson[4], Vincent Drouin[1], Thóra Árnadóttir[1], Kristín Jónsdóttir[4], Magnús T. Gudmundsson[1], Thórdís Högnadóttir[1], Hildur María Fridriksdóttir[1,4], Martin Hensch[4], Páll Einarsson[1], Eyjólfur Magnússon[1], Sergey Samsonov[5], Bryndís Brandsdóttir[1], Robert S. White[6], Thorbjörg Ágústsdóttir[6], Tim Greenfield[6], Robert G. Green[6], Ásta Rut Hjartardóttir[1], Rikke Pedersen[1], Richard A. Bennett[7], Halldór Geirsson[8], Peter C. La Femina[8], Helgi Björnsson[1], Finnur Pálsson[1], Erik Sturkell[9], Christopher J. Bean[10], Martin Möllhoff[10], Aoife K. Braiden[10] & Eva P. S. Eibl[10]

Crust at many divergent plate boundaries forms primarily by the injection of vertical sheet-like dykes, some tens of kilometres long[1]. Previous models of rifting events indicate either lateral dyke growth away from a feeding source, with propagation rates decreasing as the dyke lengthens[2–4], or magma flowing vertically into dykes from an underlying source[5,6], with the role of topography on the evolution of lateral dykes not clear. Here we show how a recent segmented dyke intrusion in the Bárðarbunga volcanic system grew laterally for more than 45 kilometres at a variable rate, with topography influencing the direction of propagation. Barriers at the ends of each segment were overcome by the build-up of pressure in the dyke end; then a new segment formed and dyke lengthening temporarily peaked. The dyke evolution, which occurred primarily over 14 days, was revealed by propagating seismicity, ground deformation mapped by Global Positioning System (GPS), interferometric analysis of satellite radar images (InSAR), and graben formation. The strike of the dyke segments varies from an initially radial direction away from the Bárðarbunga caldera, towards alignment with that expected from regional stress at the distal end. A model minimizing the combined strain and gravitational potential energy explains the propagation path. Dyke opening and seismicity focused at the most distal segment at any given time, and were simultaneous with magma source deflation and slow collapse at the Bárðarbunga caldera, accompanied by a series of magnitude $M > 5$ earthquakes. Dyke growth was slowed down by an effusive fissure eruption near the end of the dyke. Lateral dyke growth with segment barrier breaking by pressure build-up in the dyke distal end explains how focused upwelling of magma under central volcanoes is effectively redistributed over long distances to create new upper crust at divergent plate boundaries.

The formation of dykes is favourable at divergent plate boundaries, because plate movements stretch the crust and reduce the normal stress on potential dyke planes. Rifting events at divergent plate boundaries typically occur in episodes separated by hundreds of years of quiescence. Only a few such episodes have been monitored, as most divergent plate boundaries form mid-ocean ridges. In 1975–84 a rifting episode took place at Krafla volcanic system, Iceland, and from 2005 to 2010 in the Afar region of Ethiopia[1]. Limited geodetic and seismic data have been interpreted in terms of lateral flow of magma, with dyke propagation rates of up to 2–3 km per hour initially and then at a declining rate as magma propagates away from a central feeding source[2–4]. The propagation of such dykes has been modelled as inflation of magma filled cracks with uniform excess pressure[7,8]. The formation of regional dykes in Iceland has alternatively been attributed to the vertical rise of magma from major magma reservoirs underlying dyke swarms[5,6].

Bárðarbunga is a subglacial basaltic central volcano with a 70 km^2 caldera at the northwestern corner of Vatnajökull ice cap in Iceland[9,10] (Fig. 1, Extended Data Fig. 1). It has an associated fissure swarm[11] extending 115 km to the southwest and 55 km to the north-northeast. Activity in the last 2,000 years includes both subglacial eruptions and major effusive fissure eruptions, with 23 verified eruptions in the last 1,100 years[12]. Timings of the most recent effusive eruptions north of the Vatnajökull ice cap, originating from the Bárðarbunga system, are not well known, but they are inferred to have produced the Holuhraun lava field sometime in the period from AD 1794 to 1864[6]. The Holuhraun eruptive fissure was reactivated in 2014. In 1996, the Gjálp subglacial eruption was likely to have been triggered by the Bárðarbunga volcanic system[13,14]. Seismic activity at Bárðarbunga has been steadily increasing since 2005, mostly confined to the area northeast of its caldera.

On 16 August 2014 at 03:00 UTC, an intense seismic swarm began at Bárðarbunga. Initial seismic activity occurred in several clusters. One cluster was consistent with the formation of a radial dyke segment aligned in direction N127°E, outward from the Bárðarbunga caldera. Other clusters to the northeast of the caldera may also signify magma movements, or stress induced seismicity. GPS observations show simultaneous deflation of the caldera and displacements consistent with widening across the N127°E radial dyke, although deformation due to magma movements in the other clusters may also contribute. The seismic activity then focused on a lineament in direction N55°E, extending from the southern tip of the initial N127°E dyke segment (Extended Data Fig. 2). Lateral growth of this dyke is reflected in the migration of seismicity, along segments of variable strike; maximum widening of 1.3 m occurred between stations URHC and KVER spaced 25 km apart (Supplementary Fig. 1). Displacements of continuous GPS stations indicate the fastest rate of widening at any time in the most distal segment of the dyke throughout its evolution. The rate of dyke propagation varied considerably. A long halt in propagation, for 80 h, began on 19 August. Propagation rate exceeded 1 km h^{-1} on 23 August when a new segment initiated with a 90° left turn and advanced 4 km north-northwest over two short segments. Following this the dyke took a right turn onto a new lineament striking N47°E, and then onto a N25°E striking segment.

The lengthening of the dyke ended on 27 August, around 10 km north of Vatnajökull, and a minor fissure erupted in Holuhraun for about 4 h on 29 August. On 31 August, a new eruption began from the same fissure and is still ongoing at the time of writing. After 4 September the

[1]Nordic Volcanological Center, Institute of Earth Sciences, University of Iceland, IS-101 Reykjavík, Iceland. [2]Centre for the Observation and Modelling of Earthquakes and Tectonics (COMET), School of Earth and Environment, University of Leeds, Leeds LS2 9JT, UK. [3]GNS Science, PO Box 30368, Lower Hutt 5040, New Zealand. [4]Icelandic Meteorological Office, IS-150 Reykjavík, Iceland. [5]Canada Centre for Mapping and Earth Observation, Natural Resources Canada, 560 Rochester Street, Ottawa, Ontario K1A 0E4, Canada. [6]Department of Earth Sciences, University of Cambridge, Madingley Road, Cambridge CB3 0EZ, UK. [7]Department of Geosciences, University of Arizona, Tucson, Arizona 85721, USA. [8]Department of Geosciences, The Pennsylvania State University, University Park, Pennsylvania 16802, USA. [9]Department of Earth Sciences, University of Gothenburg, SE-405 30 Gothenburg, Sweden. [10]Seismology Laboratory, School of Geological Sciences, University College Dublin, Belfield, Dublin 4, Ireland.

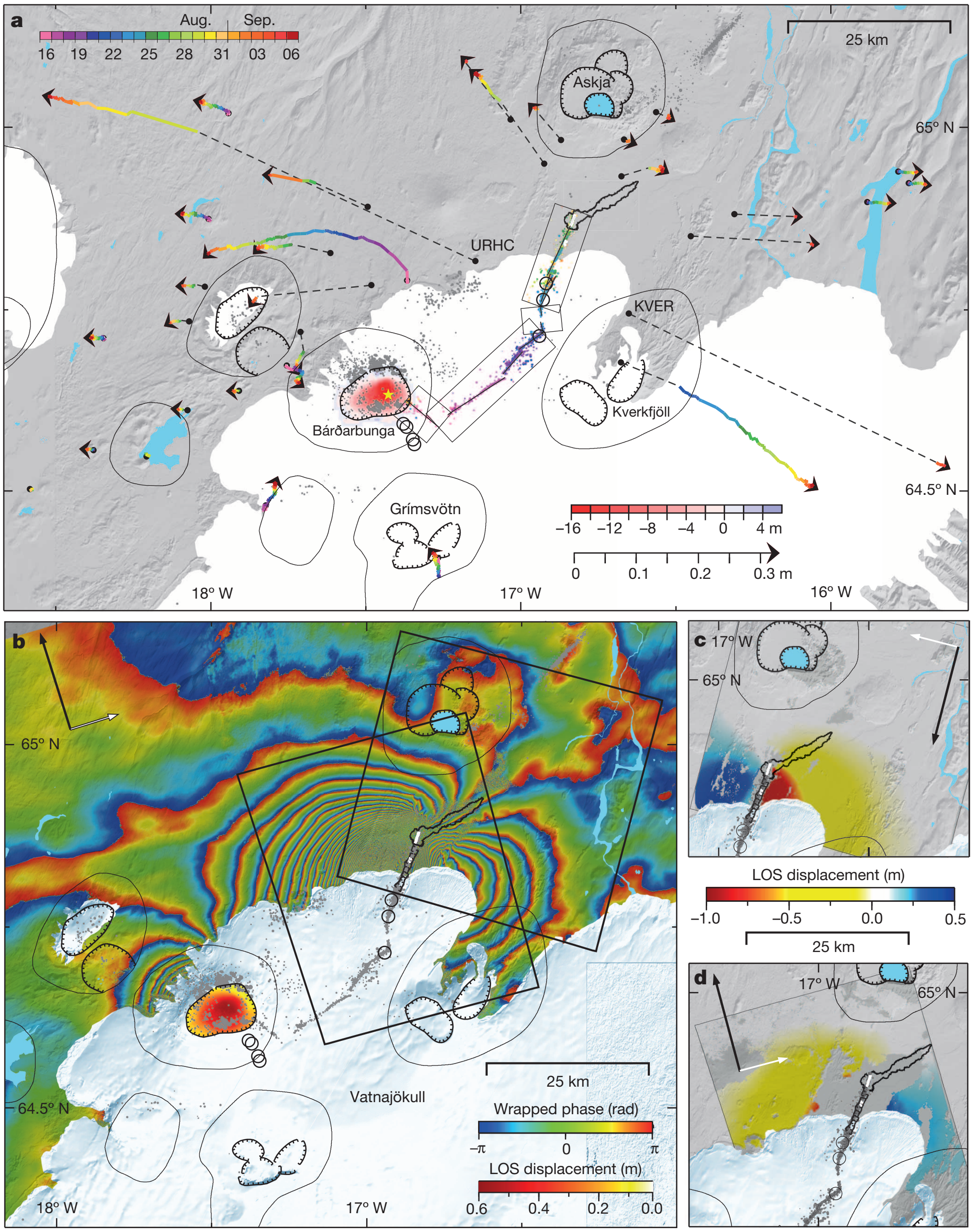

Figure 1 | Overview of data. **a**, Earthquakes 16 August to 6 September 2014 (dots) and horizontal ground displacements measured by GPS (arrows) on a map with central volcanoes (oval outlines), calderas (hatched), and northern Vatnajökull. Relatively relocated epicentres and displacements are colour coded according to time of occurrence (key at top left), other single earthquake locations are in grey. Rectangles show areas displayed in Fig. 2; thin lines within them show inferred dyke segments. The red shading at Bárðarbunga caldera shows subsidence up to 16 m inferred from radar profiling on 5 September. The star marks the location of the magma source inferred from modelling. Also shown are ice cauldrons formed (circles), outline of lava flow mapped from radar image on 6 September, and eruptive fissures (white). **b**, Wrapped RADARSAT-2 interferogram spanning 8 August to 1 September 2014. Shading at Bárðarbunga caldera shows unwrapped one day (27–28 August) COSMO-SkyMed interferogram with maximum LOS (line of sight) increase of 57 cm. Also shown are earthquakes (grey dots), boundaries of graben activated in the dyke distal area (hatched lines), and location of interferograms in **c** and **d** (boxes). **c**, Unwrapped Cosmo-SkyMed interferogram spanning 13–29 August. **d**, Unwrapped TerraSAR-X interferogram spanning 26 July 2012 to 4 September 2014. Satellite flight and viewing direction are shown with black and white arrows, respectively. LOS displacement is positive away from the satellite for all interferograms shown.

movement associated with the dyke was minor, suggesting an approximate equilibrium between inflow of magma into the dyke and magma flowing out of it feeding the eruption. Minor eruptions may have occurred under Vatnajökull; shallow ice depressions marked by circular crevasses (ice cauldrons) were discovered in the period 27 August to 7 September, indicating leakage of magma or magmatic heat to the glacier causing basal melting (Figs 1 and 2b). On 5 September, aircraft radar profiling showed that the ice surface in the centre of the Bárðarbunga caldera had subsided 16 m relative to the surroundings, resulting in a $0.32 \pm 0.08\ km^3$ subsidence bowl (Fig. 1, Extended Data Fig. 3). No evidence for basal melting was observed inside the caldera, suggesting subsidence of the caldera floor. This slow collapse of the caldera floor is considered to have started between 16 August (start of unrest) and 24 August (beginning of a series of $M \geq 5$ earthquakes in the caldera), with an average rate of subsidence in this period of up to 0.8–$1.2\ m\ d^{-1}$. It can be compared to a 1 day interferogram over the ice surface spanning 27–28 August (Fig. 1), which has a maximum line-of-sight (LOS) increase of 57 cm, indicating 55–70 cm of subsidence, over 24 h. From 24 August to 6 September, 16 $M \geq 5$ earthquakes occurred on the caldera boundary.

More than 22,000 earthquakes were automatically detected between 16 August and 6 September 2014, 5,000 of which have been manually checked. Four thousand of these have been relatively relocated, defining the dyke segments. Ground deformation in areas outside the Vatnajökull ice cap and on nunataks within the ice cap, is well mapped by a combination of InSAR, continuously recording GPS sites, and campaign GPS measurements. The GPS observations and analysis give the temporal evolution of the three-dimensional displacements used in the modelling (Fig. 1). Interferometric analysis of synthetic aperture radar images from the COSMO-SkyMed, RADARSAT-2, and TerraSAR-X satellites was used to form 11 interferograms showing LOS change spanning different time intervals (Supplementary Fig. 2). The analyses of seismic and geodetic data are described in Methods.

Initial modelling of the dyke, with no a priori constraints on position, strike or dip, shows that the deformation data require the dyke to be approximately vertical and line up with the seismicity (Extended Data Fig. 4). We therefore fixed the dip to be vertical and the lateral position of the dyke to coincide with the earthquake locations. We modelled the dyke as a series of rectangular patches and estimated the opening and

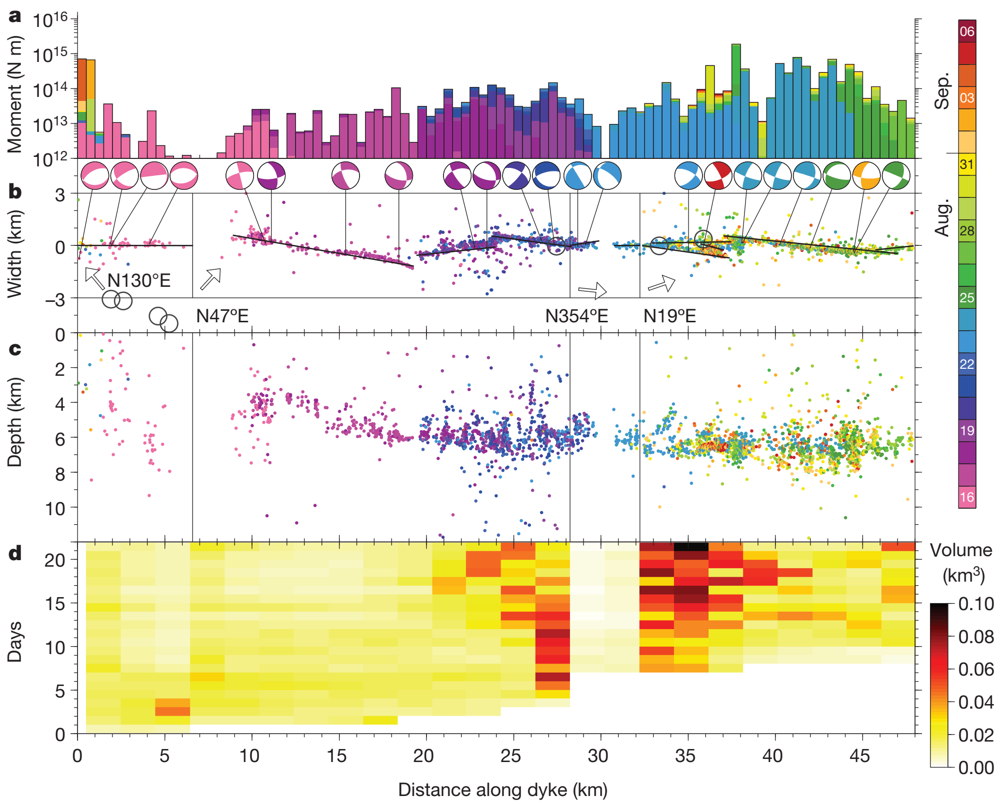

Figure 2 | Seismicity and magma volume along the dyke, 16 August to 6 September 2014. Relocated earthquakes shown in Fig. 1 are indicated, with same colour coding. **a**, Daily cumulative seismic moment at 0.5 km intervals along the dyke. **b**, Plan-view of four rotated areas along the dyke. Arrows indicate geographic north. Dots denote epicentres, black lines dyke segments, and open circles ice cauldrons. Fault-plane solutions for selected earthquakes are shown. **c**, Earthquake depths referenced to sea level. **d**, Daily vertically integrated volume of magma along the dyke inferred from geodetic modelling.

slip on each patch (Fig. 3a; see Supplementary Figs 3 and 4 for slip and standard deviations of opening). We used a Markov-chain Monte Carlo approach to estimate the multivariate probability distribution for all model parameters (Methods) on each day from 16 August to 6 September 2014 (Fig. 2d). The results suggest that most of the magma injected into the dyke is shallower than the seismicity, which mostly spans the depth range from 5 to 8 km below sea level (see Fig. 2c and Methods). While magma may extend to depths greater than 9 km near the centre of Bárðarbunga, towards the edge of the ice cap—where constraints from InSAR and GPS are much better—significant opening is all shallower than 5 km (Fig. 3a). The total volume intruded into the dyke by 28 August was 0.48–0.51 km^3.

We took two approaches to deflation models: (1) by combining GPS displacements on 4 September, interferograms ending on 3 and 4 September, respectively, and the caldera subsidence measured on 5 September; and (2) by combining all data except the caldera subsidence in a time dependent model. Our approximate model has two dip-slip faults at the boundary of the caldera and an underlying magma source; either a spherical or a flat top chamber. In approach (1), the best-fit models have a spherical chamber centred at 1.3–1.5 km depth below sea level and a volume change of 0.26–0.29 km^3, or a flat-topped chamber stretching from 3.4–3.6 km downwards and a volume change of 0.24–0.31 km^3 (Extended Data Figs 5 and 6, Supplementary Figs 5 and 6). We consider the actual volume loss at depth to be at least equal to the volume of the caldera subsidence on 5 September (0.32 ± 0.08 km^3); the volumes predicted by our simple models are marginally smaller. The time dependent models not using the caldera subsidence result in underprediction of the volume change. Inverting the GPS and InSAR data from 3 and 4 September, but neglecting the caldera subsidence measurements, results in a volume change that is smaller by a factor of 2.0. We therefore scale the estimated volumes in our time dependent models by this factor to give more reliable estimate (Fig. 4). The volume decrease beneath the caldera tracks the volume increase of the dyke for the first week of the activity. The volume decrease then decelerates to less than half the previous rate, although the dyke volume increase continues at the same rate. This suggests inflow of magma from an underlying deeper source after the first week, which is not visible in the geodetic data. Full details of the results are given in Methods and Supplementary Information.

Lateral growth of a dyke is expected to follow the minimum potential energy principle. Assuming a closed system, a dyke will tend to be emplaced such that it minimizes the total potential energy[15–17], Θ_T, given by:

$$\Theta_T = \Theta_s + \Theta_g \quad (1)$$

where Θ_s is the strain potential and Θ_g the gravitational energy potential. Evaluation of the strain energy requires knowledge of the prior stress and strain field in the crust. We consider here the role of plate movements and topography in steering the propagation path of a dyke once it is initiated; its onset point will depend on other factors, such as details of the magma plumbing system feeding it and the path of previous dykes. We approximate strain and stress due to plate movements as described in Methods, and then consider strain changes induced by the dyke formation. Opening of a dyke is energetically favourable when it releases strain energy built up at a divergent plate boundary, but once deviatoric stress in the crust adjacent to a segment is released it becomes favourable to propagate laterally. We estimate the total strain energy before and after advance of a dyke segment by numerically integrating the strain energy density over a large volume:

$$\Theta_s = \frac{1}{2}\int \sigma_{ij}\varepsilon_{ij}\,\mathrm{d}V \quad (2)$$

where σ_{ij}, ε_{ij} and $\mathrm{d}V$ are respectively the components of the stress tensor, strain tensor, and the volume element of integration[15]. We approximate the change in gravitational energy in surrounding crust, for each dyke segment, by integrating the predicted vertical displacements multiplied by the local topographic load density (ice and crust) above a reference surface and the acceleration of gravity (Methods). Dyke formation is associated with uplift on their flanks; the lower the topographic load over the flanks, the less energy it costs. For any given location on a volcano,

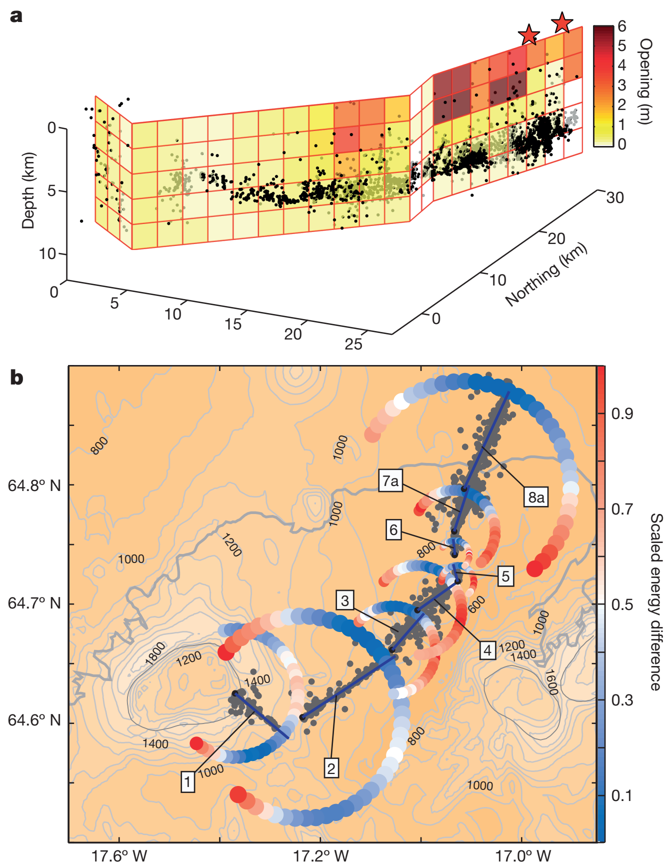

Figure 3 | Dyke model. **a**, Median of the posterior probability of opening for dyke patches inferred from modelling (key at right), and relocated earthquake hypocentres (black and grey dots, in front of and behind the dyke plane, respectively) relative to sea level. Red stars mark the eruption sites. **b**, Preferred direction of dyking for different segments based on a model of combined strain and gravitational potential energy release. Blue lines represent dyke segments and grey dots earthquake epicentres. Black dots indicate the beginning of each segment and surrounding arc of coloured points represent possible end points for different strikes of propagation. Their colour (key at right) indicates $(E - E_{\min})/(E_{\max} - E_{\min})$, where E is the energy state for a particular strike, and $E_{\min}$ and $E_{\max}$ are the respective minimum and maximum energy state for that segment. Background shows bedrock topography with calderas outlined (in black). Grey thick line shows the edge of the Vatnajökull ice cap.

the strike of a new dyke segment will influence the strain and gravitational potential energy change in a different way. The direction that minimizes the combined energy should be favoured (Methods and Extended Data Figs 7 and 8). For the Bárðarbunga 2014 rifting event, the actual propagation path closely follows that predicted by our model (Fig. 3b) and can in particular explain why the dyke propagation changed to a northerly direction after initially propagating to the southeast. The influence of topography is large during the first segments but decreases as the dyke propagates towards more level topography and the tectonic stress becomes dominant in determining the direction of the dyke propagation. In essence, the dyke is captured by the plate spreading field once it is sufficiently far from the Bárðarbunga central volcano, which is located to the west of the central axis of the plate spreading model invoked (Methods). We have assumed in our model that the dyke remains at a fixed depth with respect to sea level, as it propagates. If in fact the dyke maintains a level of neutral buoyancy, the influence of topography will be about one-third greater (Methods), changing the predicted path slightly.

Our results show the dyke is heterogeneous in terms of seismic moment release and vertically integrated magma volume, peaking on the segments where the dyke halted, at 20–28 km and 33–39 km along the

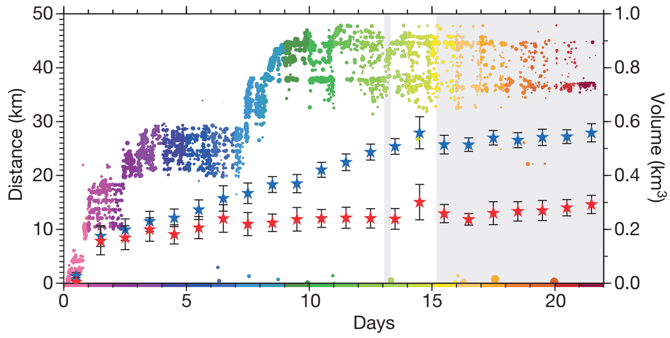

Figure 4 | Seismicity and volume change. Dots indicate earthquakes along the length of the dyke (left-hand *y* axis) as a function of time; stars, volume change (right-hand *y* axis) of the dyke (blue) and of the magma source (red). Earthquakes are colour coded by time (key along bottom), with dot radius proportional to earthquake magnitude. The volumes (error bars show 95% confidence intervals) are estimated from available geodetic data for each day using a model of a point pressure source and two dip-slip faults beneath the caldera. The magma source volumes are scaled by a factor of two, such that the value estimated for 5 September from GPS and InSAR data alone becomes equal to that estimated when the caldera subsidence is added to the inversion. Shading indicates the Holuhraun eruptions (see main text).

dyke (Fig. 2a). These are also locations where magma possibly reached the bedrock surface, as revealed by the ice cauldrons formed (Fig. 2b). The longest halt in the dyke propagation on 19–23 August correlates with increased lithostatic pressure, for any given depth, in the direction of propagation (Extended Data Fig. 8). Lateral dyke propagation is facilitated if a dyke advances into an area with falling lithostatic pressure, as the level of neutral buoyancy drops[18]. Such a process can be driven by gravity alone, but farther propagation when the lithostatic pressure increases requires the dyke to propagate upwards. Several days of magma flow to the Bárðarbunga dyke tip were required to increase the internal pressure sufficiently and drive propagation past the largest barrier along its path. Our seismic and geodetic observations provide details of a lateral dyke advance in segments, which can be related to the effects of the plate boundary stress field and topography on dyke steering and segmentation, with flow influenced by along-dyke variation in the lithostatic pressure profile. Similar studies, which may in future be carried out in near real-time, can lead to improved understanding of the evolution and forecasting of the behaviour of lateral dykes in various tectonic settings[19,20].

Online Content Methods, along with any additional Extended Data display items and Source Data, are available in the online version of the paper; references unique to these sections appear only in the online paper.

Received 8 October; accepted 25 November 2014.

Published online 15 December 2014.

1. Wright, T. J. *et al.* Geophysical constraints on the dynamics of spreading centres from rifting episodes on land. *Nature Geosci.* **5,** 242–250 (2012).
2. Einarsson, P. & Brandsdottir, B. Seismological evidence for lateral magma intrusion during the July 1978 deflation of the Krafla volcano in NE-Iceland. *J. Geophys.* **47,** 160–165 (1980).
3. Buck, W. R., Einarsson, P. & Brandsdottir, B. Tectonic stress and magma chamber size as controls on dike propagation: constraints from the 1975–1984 Krafla rifting episode. *J. Geophys. Res.* **111,** B12404, http://dx.doi.org/10.1029/2005JB003879 (2006).
4. Belachew, M. *et al.* Comparison of dike intrusions in an incipient seafloor-spreading segment in Afar, Ethiopia: seismicity perspectives. *J. Geophys. Res.* **116** (B6), B06405, http://dx.doi.org/10.1029/2010JB007908 (2011).
5. Gudmundsson, A. Infrastructure and mechanics of volcanic systems in Iceland. *J. Volcanol. Geotherm. Res.* **64,** 1–22 (1995).
6. Hartley, M. E. & Thordarson, T. The 1874–1876 volcano-tectonic episode at Askja, North Iceland: lateral flow revisited. *Geochem. Geophys. Geosyst.* **14,** 2286–2309 (2013).
7. Segall, P. *Earthquake and Volcano Deformation* (Princeton Univ. Press, 2009).
8. Segall, P., Llenos, A. L., Yun, S.-H., Bradley, A. M. & Syracuse, E. M. Time-dependent dike propagation from joint inversion of seismicity and deformation data. *J. Geophys. Res. Solid Earth* **118,** 5785–5804 (2013).

9. Björnsson, H. *Hydrology of Ice Caps in Volcanic Regions* Vol. 45 (Societas Scientarium Islandica, 1988).
10. Gudmundsson, M. T. & Högnadóttir, T. Volcanic systems and calderas in the Vatnajökull region, central Iceland, constraints on crustal structure from gravity data. *J. Geodyn.* **43,** 153–169 (2007).
11. Björnsson, H. & Einarsson, P. Volcanoes beneath Vatnajökull, Iceland: evidence from radio-echo sounding, earthquakes and jökulhlaups. *Jökull* **40,** 147–168 (1990).
12. Thordarson, T. & Larsen, G. Volcanism in Iceland in historical time: volcano types, eruption styles and eruptive history. *J. Geodyn.* **43,** 118–152 (2007).
13. Einarsson, P. *et al.* Center of the Iceland hotspot experiences volcanic unrest. *Eos* **78,** 369–375 (1997).
14. Pagli, C. *et al.* Crustal deformation associated with the 1996 Gjálp subglacial eruption, Iceland: InSAR studies in affected areas adjacent to the Vatnajökull ice cap. *Earth Planet. Sci. Lett.* **259,** 24–33 (2007).
15. Reddy, J. N. *An Introduction to Continuum Mechanics* (Cambridge Univ. Press, 2013).
16. Dahm, T. Numerical simulations of the propagation path and arrest of fluid-filled fractures in the Earth. *Geophys. J. Int.* **141,** 623–638 (2000).
17. Maccaferri, F., Bonafede, M. & Rivalta, E. A quantitative study of the mechanisms governing dike propagation, dike arrest and sill formation. *J. Volcanol. Geotherm. Res.* **208,** 39–50 (2011).
18. Fialko, Y. A. & Rubin, A. What controls the along-strike slopes of volcanic rift zones? *J. Geophys. Res.* **104,** 20007–20020 (1999).
19. Toda, S., Stein, R. S. & Sagiya, T. Evidence from the AD 2000 Izu islands earthquake swarm that stressing rate governs seismicity. *Nature* **419,** 58–61 (2002).
20. Staudacher, T. *et al.* The April 2007 eruption and the Dolomieu crater collapse, two major events at Piton de la Fournaise (La Réunion Island, Indian Ocean). *J. Volcanol. Geotherm. Res.* **184,** 126–137 (2009).

Supplementary Information is available in the online version of the paper.

Acknowledgements Support for this work was received from the European Community's Seventh Framework Programme Grant No. 308377 (Project FUTUREVOLC), the Icelandic Research Fund (Project Volcano Anatomy), the Research Fund at the University of Iceland, NERC, the Geological Survey of Ireland and the US National Science Foundation (NSF). COSMO-SkyMed data were provided by the Italian Space Agency (ASI) and TerraSAR-X data by the German Space Agency (DLR) through the Icelandic Volcanoes Supersite project supported by the Committee on Earth Observing Satellites (CEOS). RADARSAT-2 data were provided by the Canadian Space Agency and MDA Corporation. Natural Resources Canada Earth Sciences Sector contribution number 20140314. An intermediate TanDEM-X digital elevation model was provided by DLR under project IDEM_GEOL0123. We thank the following key persons for help with instrumentation and data: B. H. Bergsson, þ. Jónsson, V. H. Kjartansson, S. Steinórsson, P. Erlendsson, H. Ólafsson, J. Söring and D. Craig. We also acknowledge the many others who have contributed to GPS, seismic and other field work in the study area. For GPS equipment and support, we acknowledge services provided by the UNAVCO Facility with support from the US NSF and National Aeronautics and Space Administration (NASA) under NSF Cooperative Agreements Nos EAR-0735156 and EAR-0711446. S. Jónsson (KAUST, Saudi Arabia) and T. Villemin (EDYTEM, Université de Savoie, France) also provided support to GPS. Seismic equipment: The British Geological Survey donated several of the broadband seismic sensors around Vatnajökull. We thank the SEISUK facility for loans to R.S.W. of seismometers under loan 980. Landsvirkjun contributed GPS instruments and seismic sensors north of Vatnajökull. The surveying aeroplane of Isavia (Icelandic Aviation Operation Services) mapped the subsidence of Bárðarbunga. The Icelandic Coast Guard provided aeroplane and helicopter support for field studies.

Author Contributions The writing of the paper, and the research it is based on, was coordinated by F.S., A.H., S.H., K.S.V., B.G.Ó. and other members of Icelandic Meteorological Office (IMO) seismic monitoring team. All authors contributed ideas and input to the research and writing of the paper. Modelling of geodetic data was done by A.H., E.R.H. and Th.A. Analysis and operation of continuous GPS sites were carried out by S.H., B.G.Ó., H.M.F, R.A.B., V.D., H.G. and P.C.L. Relative earthquake locations were calculated by K.S.V., seismic data presentation and relative locations were by G.B.G., focal mechanisms were determined by M.H. and single earthquake location determination was led by K.J. and SIL seismic monitoring group. Interferometric analysis was carried out by S.D., K.S., M.P., V.D. and S.S., with a composite digital elevation model prepared by E.M. The combined strain and gravity potential in relation to the dyke propagation was modelled by E.R.H. in consultation with A.H. and F.S. Campaign GPS measurements were carried out by S.D., V. D., M.P., Á.R.H., E.S., F.S. and others. M.T.G. and Th.H. mapped the collapse of the Bárðarbunga caldera and the formation of ice cauldrons over the path of the dyke with aircraft radar profiling. Á.R.H., E.M. and P.E. led mapping of graben formed and of the eruptive fissure as shown here. P.E., B.B. and R.P. contributed to the interpretation of events, and H.B. and F.P. provided bedrock topography and ice thickness for Vatnajökull ice cap. R.S.W., Th.Á., T.G., R.G.G., C.J.B., M.M., A.K.B. and E.P.S.E. contributed and analysed seismic data.

Author Information Reprints and permissions information is available at www.nature.com/reprints. The authors declare no competing financial interests. Readers are welcome to comment on the online version of the paper. Correspondence and requests for materials should be addressed to F.S. (fs@hi.is).

METHODS

Seismic analysis. Seismicity was recorded by the Icelandic national seismic network (SIL) complemented with seismometer installations from the University of Cambridge and University College Dublin. Events attributed to the laterally growing dyke are volcano tectonic events. Initial single earthquake locations are performed by minimizing the square sum of both P- and S-wave arrival time residuals in the SIL analysis software[21]. Relative relocations are obtained by iterative inversion of the weighted square sums of: absolute P- and S-arrival time differences, as well as the double differences of (1) absolute arrival times of P and S waves, (2) relative arrival times of P and S waves and (3) relative S–P arrival times[22]. Each event is inverted in a group with over 40 of its nearest neighbours. Overlap of groups is enough to ensure that most events are located in at least five groups. The solutions shown are obtained using the SIL velocity model, which is the standard one-dimensional (1D) reference velocity model of the SIL analysis system[23]. In the relative earthquake locations, the different elevations of seismic stations are not taken into consideration, except through the relative importance of the stations in the inversion for best locations (that is, the number of phases used). The average elevation of the dominant stations (0.9 km) is therefore taken as the initial reference elevation of the relative location results. To reference the location results to sea level, the depths were therefore shifted upwards by 0.9 km. To estimate the dependence of the location results on velocity model, the relative locations were also calculated in a second velocity model (IMO-vj), which is a rough 1D approximation to the velocity on the ICEMELT refraction profile at the northern margin of Bárdarbunga[24]. This model gives source depths which are within 100 m in lateral distance but mostly around 2.5 km deeper than in the SIL model. This is probably caused by the lower velocities in the IMO-vj model below 6 km depth (Supplementary Fig. 7). Even though relative earthquake location errors can be quite small, there is always ambiguity about absolute location accuracies. The location of the ice depressions above the dyke segments where the dyke propagation temporarily stalled, and the location of the graben subsidence directly above the seismicity, confirm the quality of the absolute lateral locations. To further test the absolute depth accuracies, 100 events along the whole dyke were selected and located with NonLinLoc[25] in another approximation to the ICEMELT profile at Vatnajökull (CAM-vatnaj). The results, referenced to sea level (Supplementary Figs 7 and 8), show a very similar depth range to the relative locations and further support the absolute vertical location quality of the earthquakes. The two models, SIL and CAM-vatnaj, have a very different shallow structure, but below 6.5 km, where most of the seismicity is concentrated, they are very similar.

Focal mechanisms. These (Fig. 2) are best fitting solutions using a lower hemisphere projection based on grid search over all strike, dip and rake combinations matching observed P-wave polarities and within allowed limits from observed spectral amplitudes of P and S waves[26]. Exemplary focal mechanisms of earthquakes $M > 2$ with at least six fitting P-wave polarities have been selected for each subcluster of the dyke intrusion. Mechanisms shown in Fig. 2 are rotated according to the directions of the rotated areas along the dyke. Focal mechanisms have tensional axes consistently orientated near perpendicular to the dyke as expected near dykes[19], while pressure axes are variable depending on the location of the event with respect to the dyke (that is, above or in front of it).

GPS analysis. Significant deformation was observed at 16 pre-existing continuous GPS stations in relation to the Bárðarbunga events in 2014. Five additional sites were set up during the unrest leading up to the Holuhraun fissure eruption, all installed next to or on existing monuments (Supplementary Table 1). An additional 16 sites were measured regularly during the unrest (Supplementary Table 2). Multiple measurements were made at all these sites before the Bárðarbunga unrest, with the exception of site GSIG, which was installed and first measured in June 2014. GSIG is located about 700 m from an existing benchmark. The last pre-unrest GPS campaign in the region was conducted from 28 July to 9 August 2014.

The GPS data were analysed using the GAMIT/GLOBK software, version 10.4 (ref. 27), using over 100 global reference stations. Average site positions were evaluated in the ITRF08 reference frame every 24 h UTC day. The continuous GPS data were furthermore divided into three eight-hour sessions with a running 24 h window of reference station and orbit data, to provide higher temporal resolution (Supplementary Fig. 1a–f). In addition to station coordinates, the processing solved for satellite orbit and Earth rotation parameters, atmospheric zenith delay every two hours, and three atmospheric gradients per day. Ocean loading was corrected for using the FES2004 model. The IGS08 azimuth and elevation dependent absolute phase centre model was applied for all antennas. Pre-rifting site velocities were estimated based on all existing data and removed from the data. The last three to six days of measurements at each site before 16 August were then used to estimate a reference epoch. Data affected by snow and ice were removed during the analysis.

Interferometric analysis. This analysis of X-band satellite data (wavelength ~3.1 cm) from the COSMO-SkyMed and TerraSAR-X satellites was undertaken using the Repeat Orbit Interferometry Package (ROI_PAC)[28] and DORIS software[29]. Analysis of C-band RADARSAT-2 data (wavelength ~5.56 cm) was computed using the GAMMA software[30]. Topographic signal in the interferograms was estimated using a LiDAR DEM[31] on the glacier and for an area extending 2–3 km from the glacier margin. Further from the glacier, an intermediate DEM from the TanDEM-X mission was used with a DEM from the ASTER satellite mission and the EMISAR DEM[32] to fill in observed gaps. The DEM mosaic used for the topographic correction has a pixel size of about 13 m × 30 m (the pixel size of the ASTER DEM), at the latitude of Iceland. Interferograms were filtered using a power spectrum filter[33] and unwrapped using the branch cut algorithm[34] and the SNAPHU minimum-cost-flow method[35]. We downsampled all interferograms using an adaptive quadtree approach[36], with a cut-off variance of 10^{-3} m^2. Interferograms are shown in Supplementary Fig. 2 and a list of all interferograms used is in Supplementary Table 3.

The subsiding graben. This was mapped using high resolution radar images from the airborne radar system on board the Icelandic Coast Guard aircraft TF-SIF and photographs taken on board the same aeroplane. The photographs were also used to obtain coordinates for the eruptive fissures. The photographs were geo-referenced by comparison with older geo-referenced aerial photographs from Loftmyndir Corporation, using ArcGIS software. The radar images were geo-referenced with the LiDAR DEM[31] using MATLAB R2013a and Surfer 12 (Golden Software, Inc.).

Deformation modelling. Measurement errors were assumed to be drawn from a zero-mean Gaussian distribution and the errors in the physical model were assumed to scale up the effective measurement error. Application of Bayes' theorem gives the a posteriori probability distribution for the model parameters as

$$p(\mathbf{m},\sigma,|\mathbf{d})=K\left(\sigma^2\right)^{-N/2}\exp\left[-\frac{1}{2\sigma^2}(\mathbf{d}-\mathbf{Gm})^T\Sigma_d^{-1}(\mathbf{d}-\mathbf{Gm})\right]p(\mathbf{m})$$

where $\mathbf{m}$ is the vector of model parameters, $\mathbf{d}$ is the vector of measurements, $\mathbf{G}$ is a matrix of Green's functions mapping slip to displacements, Σ_d is the variance-covariance matrix for the measurements, σ^2 is the scaling factor due to model error, N is the number of measurements, K is a normalizing constant, and $p(\mathbf{m})$ is the a priori probability of the model parameters. The covariance of the error for each pair of InSAR measurements is calculated assuming a 1D exponential covariance function: Cov = 0.0016exp($-h$/5) m^2, where h is the distance between the measurement points in km. The model parameters are opening and strike-slip for the dyke patches[37], position and pressure decrease of a penny-shaped crack[38] or point pressure source[39], a bilinear orbital error ramp for each interferogram, and the hyperparameter σ^2. We allow for slip as well as opening, as dykes that are not perpendicular to the minimum compressive stress direction will be subject to shearing across the dyke walls[40]. We set the a priori probability to allow only positive opening and slip in the direction consistent with the regional stress field from relative plate motions. During the geodetic modelling the different elevation of geodetic stations was not taken into consideration. The initially inferred depths were therefore shifted by the average elevation of the GPS stations (1.0 km), resulting in geodetic model depths relative to sea level (shown here).

The a posteriori distribution is sampled using a Markov chain Monte Carlo algorithm, incorporating the Metropolis algorithm[41]. This involves selecting an initial value for each of the model parameters from $p(\mathbf{m})$ and calculating the likelihood function, which is the right-hand side of the equation above excluding $p(\mathbf{m})$. A trial random step is then taken within $p(\mathbf{m})$, and the new likelihood value is calculated. If the new likelihood value is greater, the step is taken and the trial model values are retained. If less, there is a chance that the step is taken, which is calculated as the ratio of the new likelihood over the old likelihood. Otherwise the old model values are retained. A new trial random step is taken, and the process is repeated until a representative sampling of the whole a posteriori distribution is built. The efficiency of this algorithm in reaching this goal depends on the maximum size of the random step that may be taken within $p(\mathbf{m})$. In order to ensure fast convergence, we perform a sensitivity test for each model parameter after every 1,000 iterations, and adjust the maximum step size such that all parameters contribute approximately equally to the change in likelihood and, as a whole, the mean chance of acceptance is approximately 50% (ref. 42).

The models of the deflation at Bárðarbunga are more uncertain than the dyke; however, whichever model we choose for the deflation, the modelled values of dyke opening do not change significantly.

Strain potential energy change. To calculate this change, associated with dyke formation, we require an estimate of tectonic stress (deviatoric stress induced by plate movements). To estimate the strain potential we assumed that the tectonic stress due to plate spreading could be estimated by an infinitely long and wide tensile dislocation below 10 km depth in an elastic half-space. Such a kinematic model has been used successfully to fit GPS observations across the plate boundary in Iceland[43]. This tensile dislocation was opened 4 m, which would correspond to stress built up by plate spreading for more than 200 years. It was located so that it would be under the Askja central volcano as geodetic measurements have indicated that the central axis of plate spreading passes through there[44]. The strike of this dislocation was set to N12°E, to be about perpendicular to direction of plate movements predicted by global plate motion models. We assume the tectonic stress throughout the depth interval of the crust considered does not vary with depth, similarly to the approach of Buck *et al.*[3]. The value of stress we use is that calculated at 10 m depth in the dislocation model. We calculate the stress and strain due to a dyke segment opening in a similar manner and superpose them on the estimated tectonic contributions. Assuming a linear relationship between stress and strain, we then calculate the strain energy potential using equation (2).

Gravitational potential energy change. This quantity is here calculated, for each dyke segment, as described in the text by integrating the predicted vertical displacements associated with the dyking, multiplied by the local topographic load density (ice and crust) above an arbitrary reference surface (taken here as sea level) and the acceleration of gravity. Two digital elevation models are used, one of which covers the surface of the Vatnajökull ice cap and extends beyond the limits of the ice cap, and the other which represents the ice thickness. The map of the sub-ice topography was compiled from continuous ice thickness profiling by radio echo-sounding along a series of traverses over the ice cap[9,11]. Along the complete length of the dyke the change in lithostatic pressure corresponds to an effective crustal load change of about 900 m (Extended Data Fig. 8). However, variations in the effective load in areas adjacent to an individual dyke segment influenced by vertical displacements are much smaller, typically on the order of several hundred metres or less. This is an order of magnitude less than the 2 km depth to the top of a 'test dyke segment' used for calculation of the preferred path of dyking (see below). Thus, we can consider small perturbations to the vertical deformation field introduced by the real topography to be second order.

When inferring the path of preferred dyke propagation, we assume also that the dyke depth, with respect to sea level, is the same for all strikes tested. In reality the dyke may track the level of neutral buoyancy, resulting in the preferred depth of dyking varying with strike. In our approach, the dyke moving down by one metre (with respect to sea level) can be considered equivalent to increasing the load on the reference surface by one metre of crust. The associated increase in potential energy change (compared to that when the dyke stays at the same depth) will be equal to the integrated vertical displacement of the reference surface multiplied by the density of the crust and gravitational acceleration. On the other hand, the reduction in potential energy from lowering the magma will be equal to the volume of the dyke multiplied by the density of the magma and gravitational acceleration. For a Poisson's ratio of 0.25, the integrated surface uplift is 75% of the dyke volume[45]. Therefore ~25% less energy is needed to lift the extra crust than is released by lowering the dyke. That is, the energy released in lowering the dyke is ~33% more than needed to lift the extra crust. This means that if the dyke propagates at a level of neutral buoyancy, rather than remaining at a fixed depth (with respect to sea level), the differences in gravitational potential energy change with strike will be ~33% larger than we calculate, thus increasing the influence of topography still further.

Calculation of the preferred path of dyking. For combined potential energy change during dyking, we here estimate all parameters based on seismic and geodetic data except the strike of a dyke segment. Each segment, whose location and length are determined from relative earthquake locations, is assumed to be a rectangular tensile dislocation[36]. The depth to the top of each dislocation is fixed to 2 km for all segments, the width (height) is fixed to 4 km and opening is fixed to 3 m. The starting point of each segment is fixed adjacent to the previous segment (black dots on Fig. 3b). This ensures that only energy states which assume continuation of the magma flow are considered. Then the strike of the segment is varied so that it is rotated around its starting point. The strike is varied well over 180° in search of the minimum energy for emplacement of the new segment. To implement the approach we performed two integrations, one in three dimensions for the strain potential energy and one in two dimensions for the gravitational potential energy. A Monte Carlo numerical integration in MATLAB was used, where a mean value was estimated and multiplied by the volume for strain energy, or area for gravitational energy. The rectangular dislocation formula does not take into account the strength of the material and in its vicinity the strain energy density is non-realistic and close to singular values. To avoid these values we assigned zero to energy density values over three orders of magnitude larger than the estimated average value. Therefore, we did not evaluate the strain energy densities in the immediate vicinity of a dyke intrusion, but rather evaluated how tectonically stressed crust will respond to dyke opening and if that opening will increase or decrease the total potential energy of the crust. The area of integration included a radius greater than 50 km from each dyke segment. The strain energy density was integrated down to a depth of 20 km. We found that this was sufficient so that the boundaries did not influence the estimated energy changes. To calculate the stress and strain tensors as well as the vertical surface displacements we used disloc3d, software developed by the Crustal Deformation and Fault Mechanics research group at Stanford University.

21. Böðvarsson, R., Rögnvaldsson, S. T., Slunga, R. & Kjartansson, E. *The SIL Data Acquisition System — At Present and Beyond Year 2000* (Report VÍ-R98005-JA04, Icelandic Meteorological Office, 1998).
22. Slunga, R., Rögnvaldsson, S. Th. & Bödvarsson, R. Absolute and relative locations of similar events with application to microearthquakes in southern Iceland. *Geophys. J. Int.* **123,** 409–419 (1995).
23. Stefánsson, R. *et al.* Earthquake prediction research in the South Iceland seismic zone and the SIL project. *Bull. Seismol. Soc. Am.* **83,** 696–716 (1993).
24. Darbyshire, F. A., Bjarnason, I. Th., White, R. S. & Flóvenz, Ó. G. Crustal structure above the Iceland mantle plume imaged by the ICEMELT refraction profile. *Geophys. J. Int.* **135,** 1131–1149 (1998).
25. Lomax, A., Virieux, J. J., Volant, P. & Berge, C. in *Advances in Seismic Event Location* (eds Thurber, C. H. & Rabinowitz, N.) 101–134 (Kluwer, Amsterdam, 2000).
26. Rögnvaldsson, S. T. & Slunga, R. R. Routine fault plane solutions for local networks: a test with synthetic data. *Bull. Seismol. Soc. Am.* **83,** 1232–1247 (1993).
27. Herring, T., King, R. W. & McCluskey, S. M. *Introduction to GAMIT/GLOBK Release 10.4* (Massachusetts Institute of Technology Technical Report, Cambridge, 2010).
28. Rosen, P. A., Henley, S., Peltzer, G. & Simons, M. Updated repeat orbit interferometry package released. *Eos Trans. AGU* **85,** 47 (2004).
29. Kampes, B. *Delft Object-oriented Radar Interferometric Software: User's Manual and Technical Documentation v4.02* (Delft Technical University, 1999).
30. Werner, C. *et al.* Gamma SAR and interferometric processing software. *Proc. ERS-ENVISAT Symp*. Vol. 461 (European Space Agency Special Publication, 2000).
31. Jóhannesson, T. *et al.* Ice-volume changes, bias-estimation of mass-balance measurements and changes in subglacial water bodies derived by LiDAR-mapping of the surface of Icelandic glaciers. *Ann. Glaciol.* **54,** 63–74 (2013).
32. Magnússon, E., Björnsson, H., Dall, J. & Pálsson, F. Volume changes of Vatnajökull ice cap, Iceland, due to surface mass balance, ice flow, and subglacial melting at geothermal areas. *Geophys. Res. Lett.* **32,** L05504, http://dx.doi.org/10.1029/2004GL021615 (2005).
33. Goldstein, R. R. & Werner, C. Radar interferogram filtering for geophysical applications. *Geophys. Res. Lett.* **25,** 4035–4038 (1998).
34. Goldstein, R., Zebker, H. & Werner, C. Satellite radar interferometry-two-dimensional phase unwrapping. *Radio Sci.* **23,** 713–720 (1988).
35. Chen, C. W. & Zebker, H. A. Two-dimensional phase unwrapping with use of statistical models for cost functions in nonlinear optimization. *J. Opt. Soc. Am.* **18,** 338–351 (2001).
36. Decriem, J. *et al.* The 2008 May 29 earthquake doublet in SW Iceland. *Geophys. J. Int.* **181,** 1128–1146 (2010).
37. Okada, Y. Internal deformation due to shear and tensile faults in a half-space. *Bull. Seismol. Soc. Am.* **82,** 1018–1040 (1992).
38. Fialko, Y., Khazan, Y. & Simons, M. Deformation due to a pressurized horizontal circular crack in an elastic half-space, with applications to volcano geodesy. *Geophys. J. Int.* **146,** 181–190 (2001).
39. Mogi, K. Relations between the eruptions of various volcanoes and the deformations of the ground surfaces around them. *Bull. Earthq. Res. Inst. Univ. Tokyo* **36,** 99–134 (1958).
40. Hooper, A. *et al.* Increased capture of magma in the crust promoted by ice-cap retreat in Iceland. *Nature Geosci.* **4,** 783–786 (2011).
41. Mosegaard, K. & Tarantola, A. Monte Carlo sampling of solutions to inverse problems. *J. Geophys. Res.* **100,** 12431–12447 (1995).
42. Hooper, A. *et al.* Importance of horizontal seafloor motion on tsunami height for the 2011 M_w=9.0 Tohoku-Oki earthquake. *Earth Planet. Sci. Lett.* **361,** 469–479 (2013).
43. Árnadóttir, T., Jiang, W., Feigl, K. L., Geirsson, H. & Sturkell, E. Kinematic models of plate boundary deformation in southwest Iceland derived from GPS observations. *J. Geophys. Res.* **111,** B07402, http://dx.doi.org/10.1029/2005JB003907 (2006).
44. Sturkell, E. & Sigmundsson, F. Continuous deflation of the Askja caldera Iceland, during the 1983-1998 non-eruptive period. *J. Geophys. Res.* **105,** 25671–25684 (2000).
45. Delaney, P. T. & McTigue, D. F. Volume of magma accumulation or withdrawal estimated from surface uplift or subsidence, with application to the 1960 collapse of Kilauea volcano. *Bull. Volcanol.* **56,** 417–424 (1994).
46. Jóhannesson, H. & Sæmundsson, K. *Geological Map of Iceland, Tectonics* 1:600.000 (Icelandic Institute of Natural History, 2009).
47. Gudmundsson, M. T., Högnadóttir, þ., Kristinsson, A. B. & Gudbjörnsson, S. Geothermal activity in the subglacial Katla caldera, Iceland, 1999-2005, studied with radar altimetry. *Ann. Glaciol.* **45,** 66–72 (2007).
48. Yun, S., Segall, P. & Zebker, H. Constraints on magma chamber geometry at Sierra Negra Volcano, Galápagos Islands, based on InSAR observations. *J. Volcanol. Geotherm. Res.* **150,** 232–243 (2006).

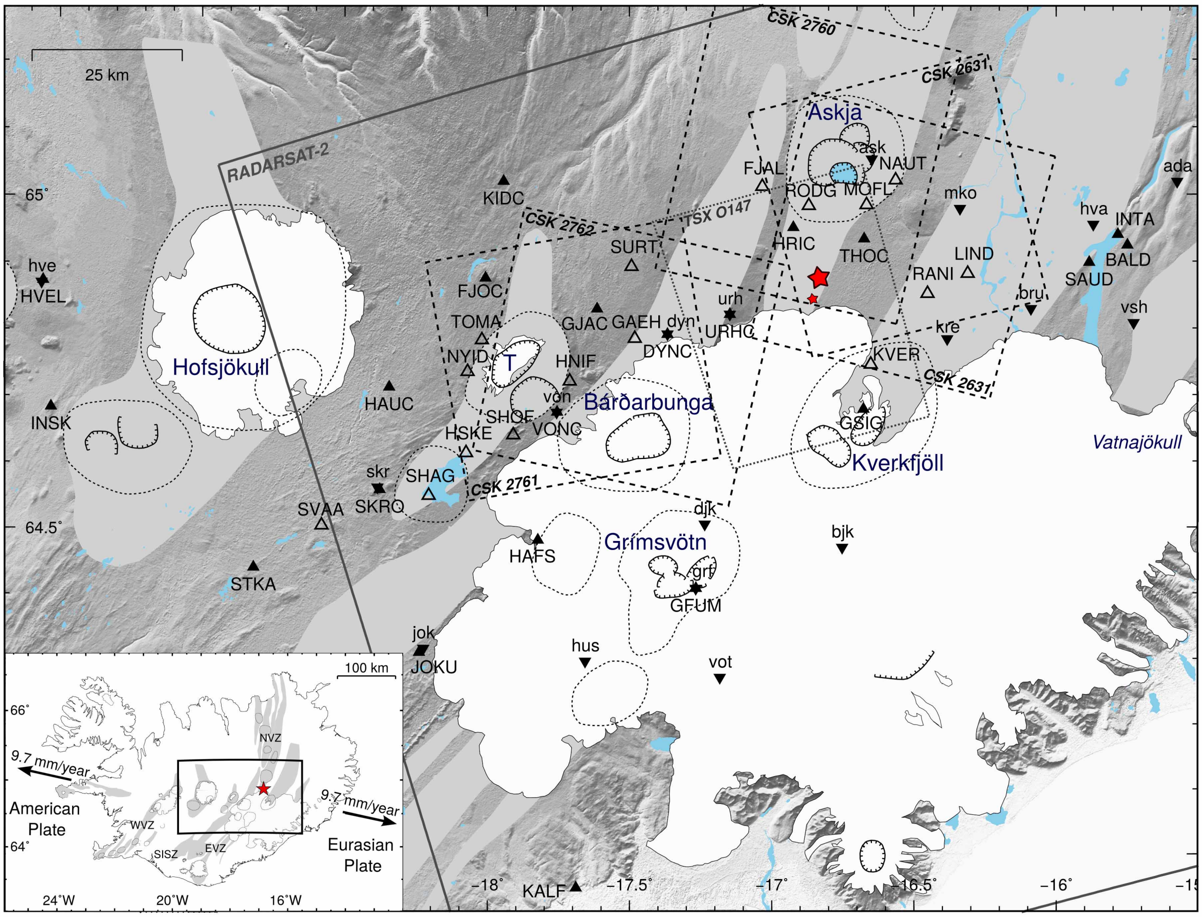

Extended Data Figure 1 | Tectonic map showing seismic and geodetic stations. Filled uptriangles correspond to continuous GPS stations, open triangles to campaign GPS sites, filled downtriangles correspond to seismic stations, and black 'stars' correspond to co-located GPS and seismic stations. Station names for GPS are indicated with four upper-case letters and for seismic stations with three lower-case letters. The different tracks for SAR satellite data are plotted with solid lines for RADARSAT-2, dashed lines for COSMO-SkyMed (CSK) and dotted lines for TerraSAR-X (TSX). Orbit numbers are indicated for CSK and TSX. The red stars correspond to the 2014 eruptive fissures at Holuhraun. Background map shows ice caps (white), central volcanoes (dotted lines), calderas (hatched lines) and fissure swarms (grey shading)[46]. Names of selected volcanoes are shown, and T indicates Tungnafellsjökull central volcano. Inset, locations of the Eastern Volcanic Zone (EVZ), the Western Volcanic Zone (WVZ), the Northern Volcanic Zone (NVZ) and the South Iceland Seismic Zone (SISZ), with their fissure swarms and central volcanoes; box shows area of the main figure.

a

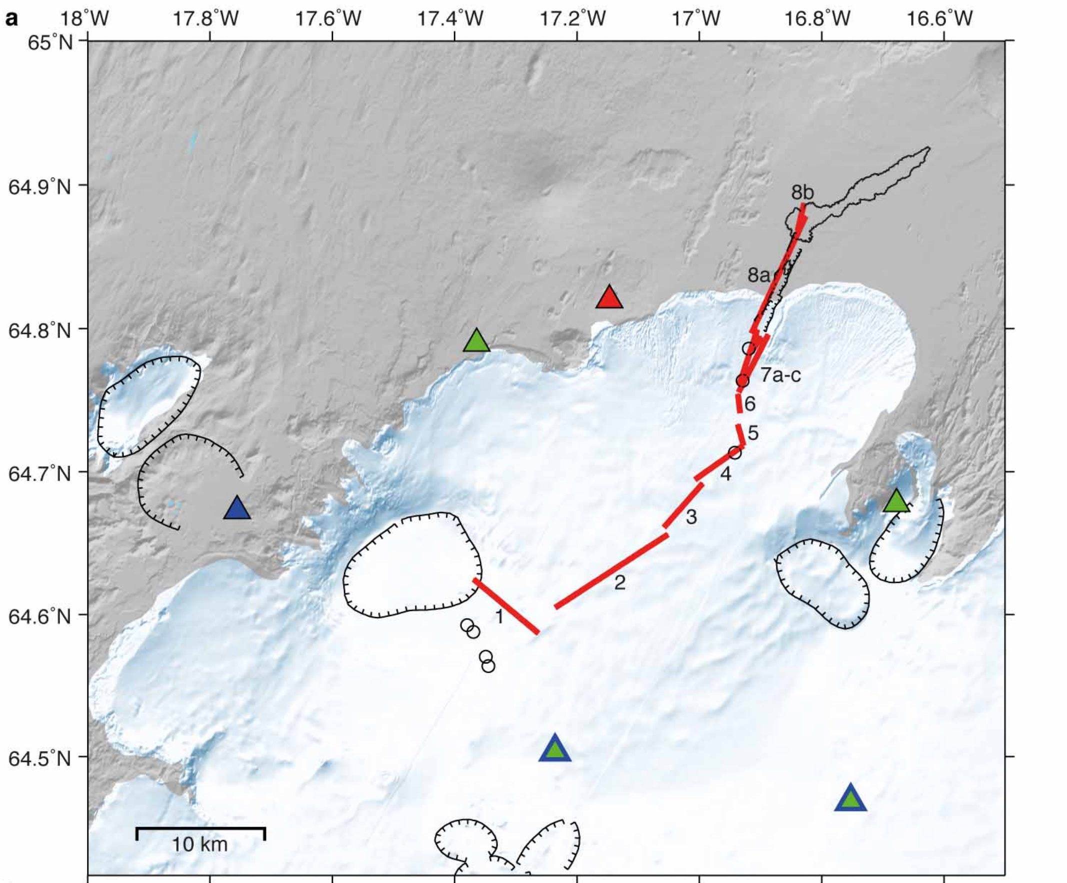

b

Nr	Lat1 °N	Lon1 °E	Lat2 °N	Lon2 °E	L km	D km	Strike °	Dip °	RMS m	# Eq
1	64.6253	-17.3693	64.5873	-17.2630	5.2	0.0 – 7.5	127	89	177.7	71
2	64.6052	-17.2359	64.6566	-17.0515	10.0	3.5 – 6.5	55	87	103.8	343
3	64.6616	-17.0579	64.6923	-16.9947	4.6	4.0 – 7.0	219	89	118.6	365
4	64.6950	-17.0074	64.7189	-16.9279	4.8	3.0 – 7.5	53	89	81.2	427
5	64.7189	-16.9279	64.7336	-16.9371	1.7	5.0 – 6.5	-11	87	75.6	70
6	64.7414	-16.9334	64.7548	-16.9368	1.4	5.0 – 6.5	173	85	58.5	60
7a	64.7560	-16.9358	64.7963	-16.8873	4.9	5.0 – 7.0	47	87	82.6	404
7b	64.7611	-16.9349	64.7998	-16.9052	4.2	4.0 – 7.0	199	89	92.0	161
7c	64.7844	-16.9148	64.7949	-16.8987	1.1	6.0 – 7.0	35	83	69.9	215
8a	64.7970	-16.9150	64.8787	-16.8262	9.7	5.0 – 8.0	25	89	200.6	1181
8b	64.8685	-16.8393	64.8878	-16.8287	1.7	5.5 – 7.0	18	85	74.1	57

Extended Data Figure 2 | Map and table of dyke segments defined by seismicity. **a**, Location of dyke segments (red lines labelled with numbers) delineated by relatively relocated earthquakes. The triangles show locations of the nearest seismic stations used to locate the events. Green, stations operated by the Icelandic Meteorological Office (IMO); blue, station operated by the University of Cambridge; and red, station operated by University College Dublin. The two stations on the ice are joint IMO and University of Cambridge stations. All stations telemetered data to IMO. Also shown are ice cauldrons formed (circles), outline of lava flow mapped from radar image on 6 September, and boundaries of graben activated in the dyke distal area (hatched lines). **b**, The dyke segments. Columns show segment number (Nr), latitude and longitude of beginning (Lat1, Lon1) and end points (Lat2, Long2) of each segment, segment length (*L*), depth range (*D*), strike, dip, the RMS value of the deviation (in metres) of the earthquakes from the plane they define, and the number of earthquakes used to define each dyke segment plane (#Eq).

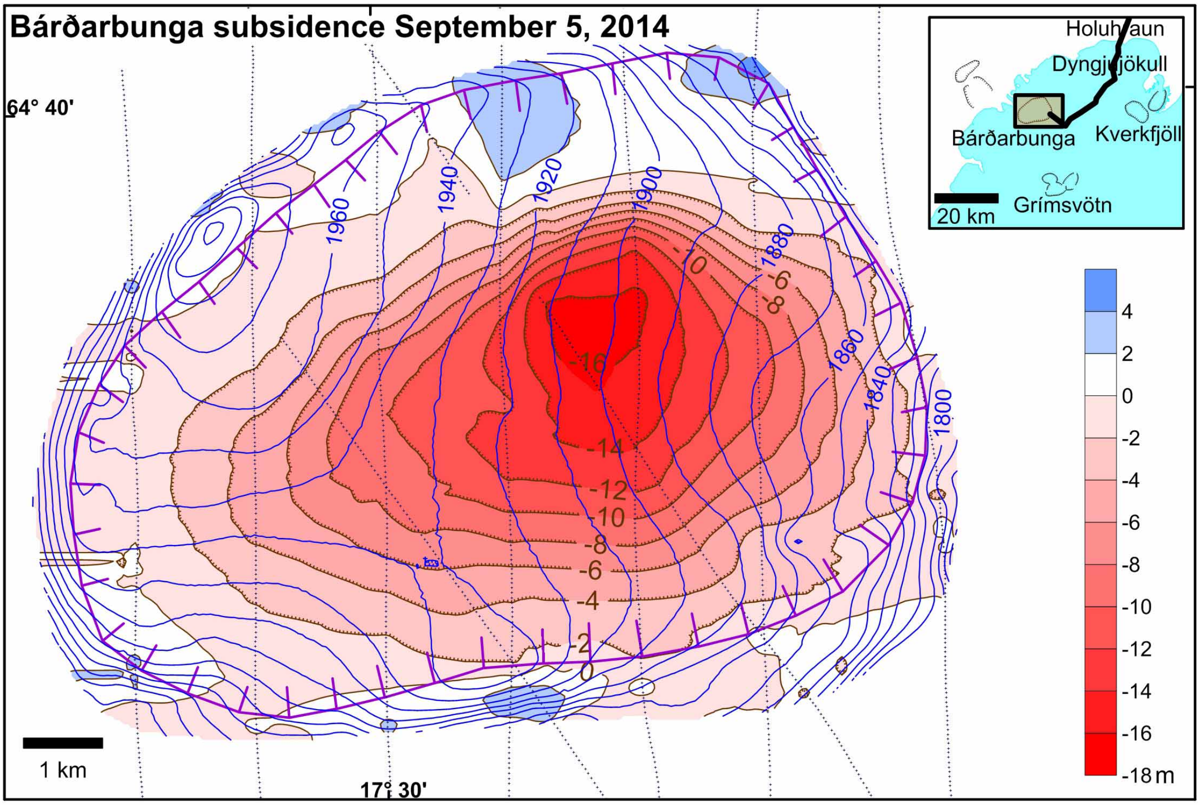

Extended Data Figure 3 | Subsidence at Bárðarbunga volcano revealed by aeroplane radar profiling. Blue contours show the elevation of the ice surface in the Bárðarbunga caldera on 5 September 2014, about three weeks after the onset of unrest. The data were obtained using aircraft flown 100–150 m above glacier surface, using radar altimetry and submetre differential GPS Omnistar. The system provides 2 m absolute accuracy of surface elevation along the survey profiles[47], shown as black dotted lines. The subsidence relative to the pre-unrest ice surface is indicated with coloured shading (key at right). It is greatest in the central part of the caldera, where it had a maximum of 16 m.

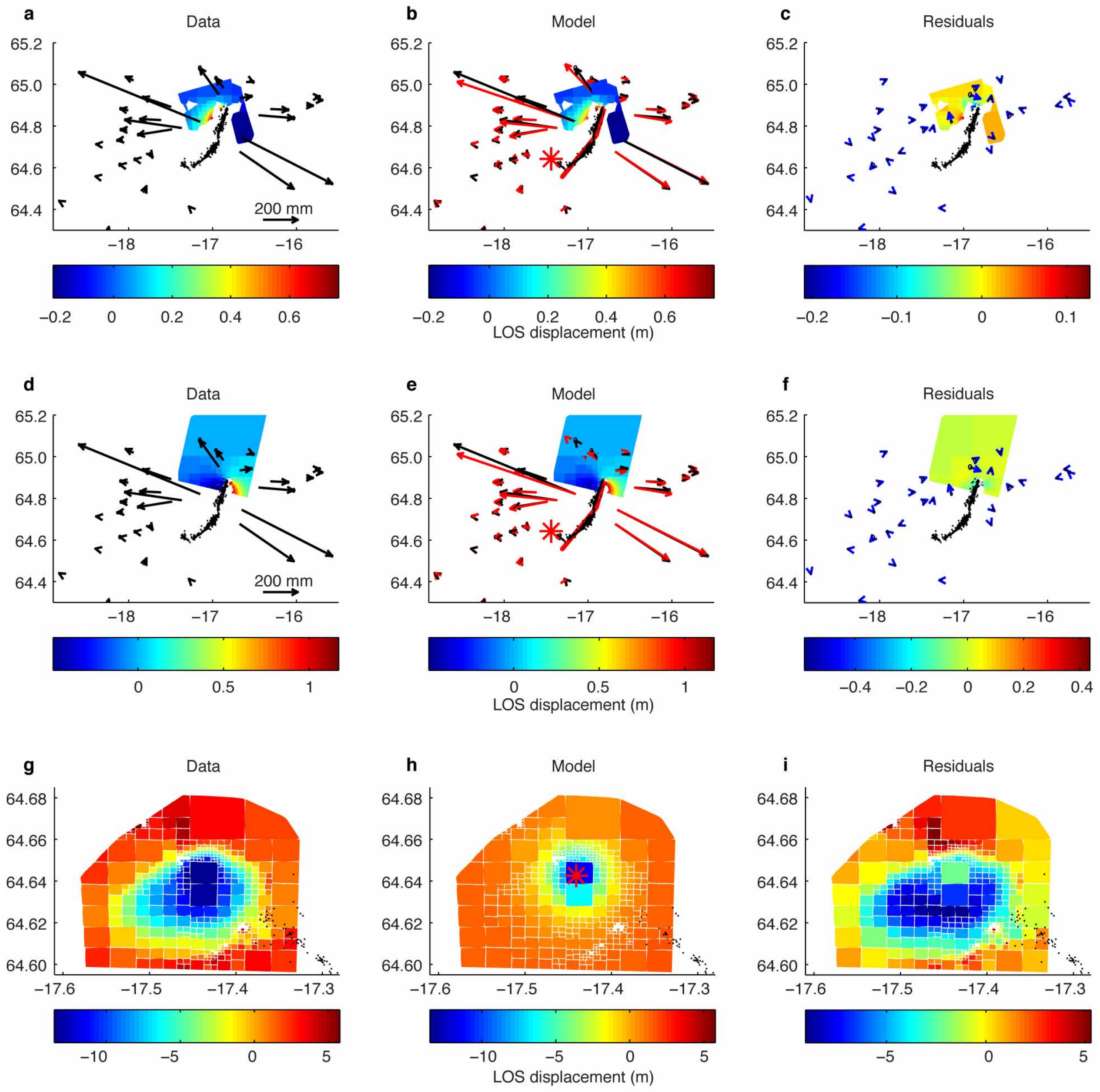

Extended Data Figure 4 | Geodetic model with a contracting point pressure source, a two-segment-dyke and no a priori constraints. The dyke segments are rectangular with uniform opening[37] and the model shown is that with maximum probability. Free parameters are: position and volume change of the point pressure source[39], and position, strike, dip and opening of the dyke. The panels show from left to right: data (**a**, **d**, **g**), model (**b**, **e**, **h**) and residuals (**c**, **f**, **i**). GPS data in all panels span 15 August to 4 September 2014. The top row shows an interferogram spanning 6 July 2012 to 4 September 2014; the middle row shows an interferogram spanning 2 August to 3 September 2014; the bottom row shows the data from Extended Data Fig. 3 from aeroplane radar profiling, but these data were not used to constrain the model.

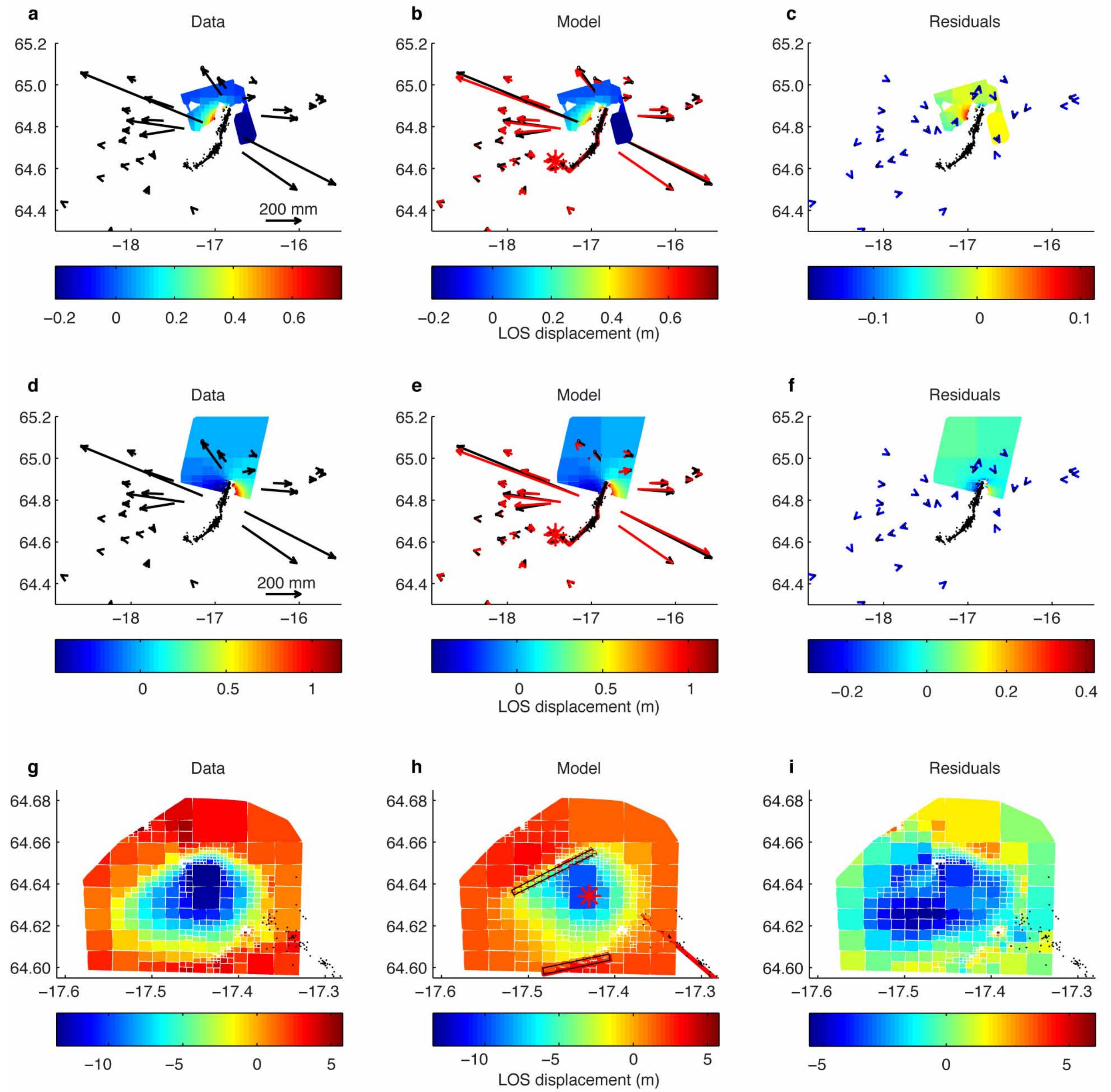

Extended Data Figure 5 | Geodetic model with a contracting point pressure source, two caldera faults, and a four-segment dyke. The dyke is divided into multiple rectangular patches[37] and the model shown is that with maximum probability. Lateral dyke position is fixed from relocated seismicity. Position of the point source and faults, volume change of the point source and opening and strike-slip of the dyke are free parameters. Left column (**a**, **d**, **g**), data; middle column (**b**, **e**, **h**), model; right column (**c**, **f**, **i**), residuals. The data are detailed in Extended Data Fig. 4 and all of the data were used to constrain the model.

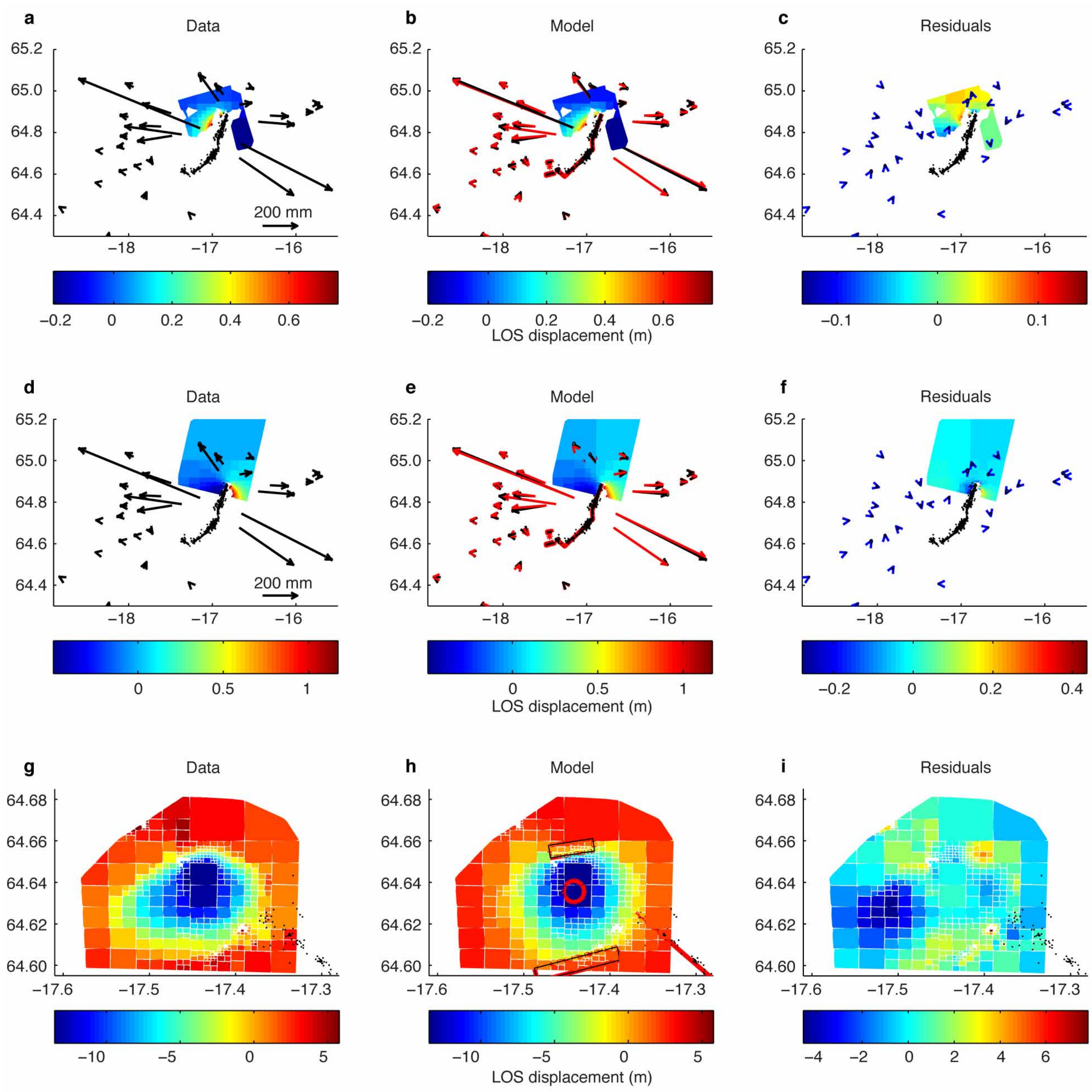

Extended Data Figure 6 | Geodetic model with a contracting flat-topped chamber, two caldera faults, and a four-segment dyke. A deflating penny-shaped crack[38] is used to represent the top of a flat-topped chamber[48], and the dyke is divided into multiple rectangular patches[37]. The model shown is that with maximum probability. Lateral dyke position is fixed from relocated seismicity. Position of the crack and faults, volume change and radius of the crack and opening and strike-slip of the dyke are free parameters. Left column (**a**, **d**, **g**), data; middle column (**b**, **e**, **h**), model; right column (**c**, **f**, **i**), residuals. The data are detailed in Extended Data Fig. 4 and all of the data were used to constrain the model.

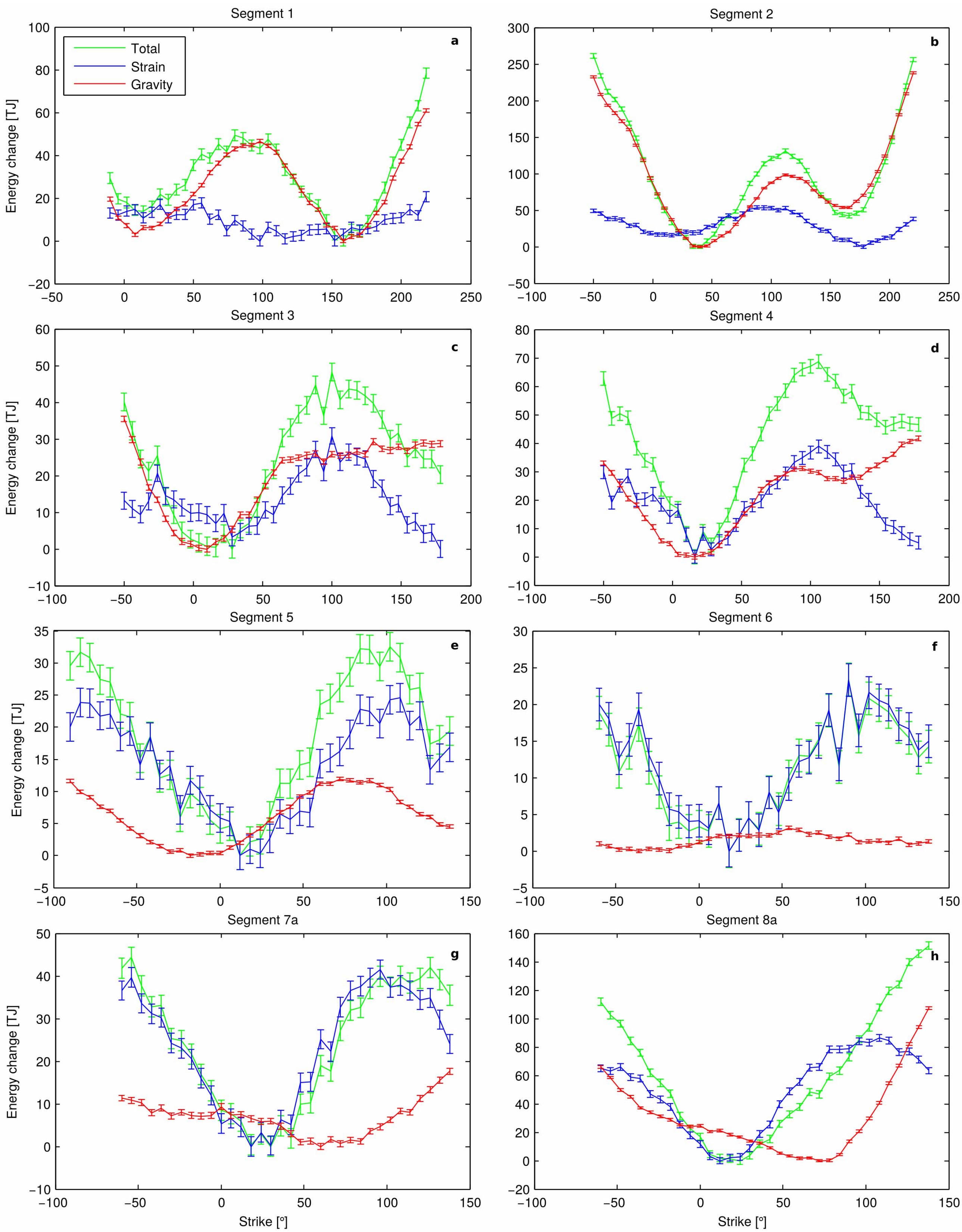

Extended Data Figure 7 | Path of dyke propagation from energy considerations. a–h, Energy profiles for dyke segments 1, 2, 3, 4, 5, 6, 7a and 8a, as described in Fig. 3b. Blue lines indicate the strain energy potential change as a function of the strike, and the red lines the gravitational potential change. Green is the total potential energy change. Energy is shown in terajoules (10^{12} J). The lowest point on each energy curve is defined as 0 TJ. Error bars, 1 s.d. of the error in the numerical integration.

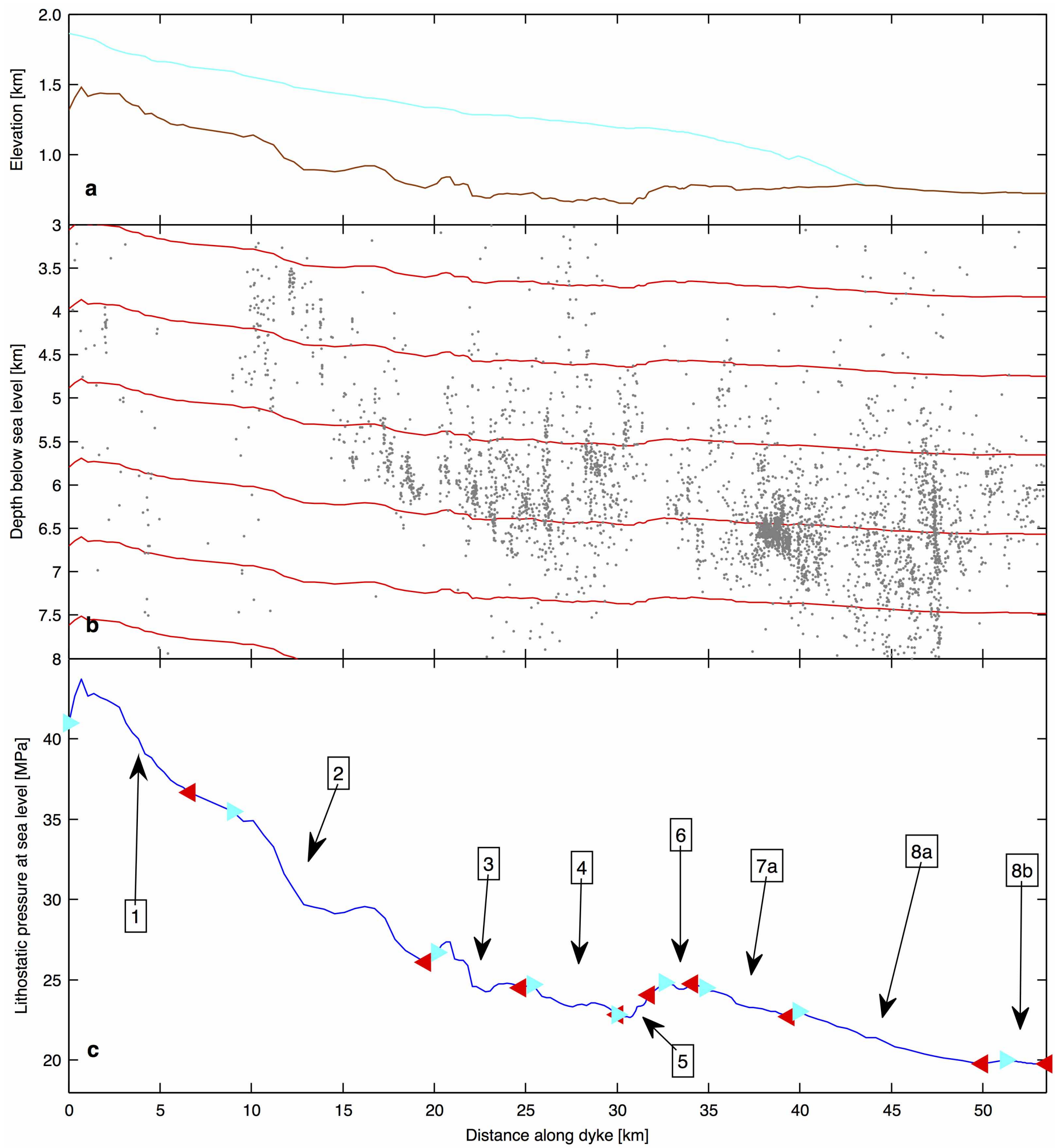

Extended Data Figure 8 | Topography, earthquake depths, and lithostatic pressure along the dyke path. **a**, Bedrock (brown line) and ice topography (light blue line) along the dyke path. **b**, Depth of earthquake hypocentres (grey dots) below sea level projected on the dyke segments and lines (red) of constant lithostatic pressure, assuming constant crustal density of 2,800 kg m^{-3} and ice density of 920 kg m^{-3}. Line spacing corresponds to 25 MPa. **c**, Lithostatic pressure at sea level calculated along dyke segments 1, 2, 3, 4, 5, 6, 7a, 8a and 8b (blue line). The calculations take into account both the subglacial bedrock topography and ice thickness. Light blue triangles indicate the beginning of a segment and red triangles the end of a segment. It is assumed that between segments the dyke propagates along a straight path. Dyke propagation was halted for the longest time at the end of segment 4 (see Figs 2 and 4), before an increase in lithostatic pressure.